Title

In Vivo Elasticity Mapping of Posterior Ocular Layers Using Acoustic Radiation Force Optical Coherence Elastography

Journal

Investigative Ophthalmology & Visual Science, 59(1)

ISSN

0146-0404

Authors

Qu, Yueqiao

He, Youmin

Saidi, Arya

et al.

Publication Date

2018-01-24

DOI

10.1167/iovs.17-22971

In Vivo Elasticity Mapping of Posterior Ocular Layers Using Acoustic Radiation Force Optical Coherence Elastography

Yueqiao Qu,[1] Youmin He,[1] Arya Saidi,[1,2] Yihang Xin,[1] Yongxiao Zhou,[1] Jiang Zhu,[1] Teng Ma,[3] Ronald H. Silverman,[4] Don S. Minckler,[5] Qifa Zhou,[3] and Zhongping Chen[1]

[1]Beckman Laser Institute, University of California, Irvine, Irvine, California, United States
[2]Marshall B. Ketchum University. Southern California College of Optometry, Fullerton, California, United States
[3]Roski Eye Institute, Department of Ophthalmology and Biomedical Engineering, University of Southern California, Los Angeles, California, United States
[4]Department of Ophthalmology, Columbia University Medical Center, New York, New York, United States
[5]Gavin Herbert Eye Institute, University of California, Irvine, Irvine, California, United States

Correspondence: Zhongping Chen, Beckman Laser Institute, University of California, Irvine, 1002 Health Sciences Road, Irvine, CA 92617, USA;
z2chen@uci.edu.

YQ and YH contributed equally to the work presented here and should therefore be regarded as equivalent authors.

Submitted: September 12, 2017
Accepted: December 17, 2017

Citation: Qu Y, He Y, Saidi A, et al. In vivo elasticity mapping of posterior ocular layers using acoustic radiation force optical coherence elastography. *Invest Ophthalmol Vis Sci*. 2018;59:455–461. https://doi.org/10.1167/iovs.17-22971

Purpose. We used acoustic radiation force optical coherence elastography (ARF-OCE) to map out the elasticity of retinal layers in healthy and diseased in vivo rabbit models for the first time.

Methods. A healthy rabbit eye was proptosed and imaged using ARF-OCE, by measuring the tissue deformation after an acoustic force is applied. A diseased retinal inflammation model was used to observe the contrast before and after disease formation. Retinal histologic analysis was performed to identify layers of the retina corresponding with the optical images.

Results. The general trend of the retinal layer elasticity is increasing stiffness from the ganglion side to the photoreceptor side, with the stiffest layer being the sclera. In a healthy rabbit model, the mechanical properties varied from 3 to 16 kPa for the five layers that were identified via optical imaging and histology (3.09 ± 0.46, 3.82 ± 0.88, 4.53 ± 0.74, 6.59 ± 2.27, 16.11 ± 5.13 kPa). In the diseased model, we have induced optical damage in a live rabbit and observed a change in the stiffness trend in its retina.

Conclusions. High sensitivity elasticity maps can be obtained using the ARF-OCE system to differentiate different retinal layers. Subtle changes in the mechanical properties during the onset of diseases, such as retinal degeneration, can be measured and aid in early clinical diagnosis. This study validates our imaging system for the characterization of retinal elasticity for the detection of retinal diseases in vivo.

Keywords: optical imaging, elasticity mapping, acoustic radiation force

Age-related macular degeneration (AMD) is a slow process whereby layers and structures in the central retina, including the macula, become progressively altered or simply waste away, leading to central vision loss or visual distortions. AMD is the number one cause of blindness in the Western world among those over the age of 50.[1,2] While age is the greatest contributing factor, other risk factors include being white or female, exposure to certain light wavelengths, history of cardiovascular disease, smoking, and so forth.[1] The most common form of AMD is known as dry/nonexudative AMD, which presents with drusen, which are composed of oxidized nondegradeable material (mostly lipofuscin) that develops between Bruch's membrane and the RPE layers of the retina. In the early stages of dry AMD, the patient may have metamorphopsia, reduced vision, or be completely asymptomatic; thus, the variable presentations highlight the need for the earliest detection methods.[1,3,4]

Since no cure currently exists for AMD, several imaging modalities and techniques are used in AMD detection and monitoring, including fundus autofluorescence (FAF), fundus photography, optical coherence tomography (OCT), fluorescein angiography, indocyanine green angiography, and Amsler grid, and so forth.[1,5,6] FAF relies on the fluorescence pattern of the oxidation compound lipofuscin contained in high amounts in the drusen.[7] OCT can identify abnormal blood vessel formation in wet AMD through OCT angiography.[1,8] Although these imaging modalities and techniques provide crucial information for the diagnosis of AMD, they often are insufficient for early diagnosis, before structural changes occur.

It recently has been shown that the mechanical properties of distinct cellular layers in the retina are altered with the onset of AMD.[9] Mechanical testing of the retina has been performed ex vivo to identify the elastic modulus of the retina.[10,11] However, this has been challenging with thin layers in the micrometer range, and without perturbing the natural retinal environment.

Elastography, the display of the elastic properties of soft tissues, may be performed using ultrasound, magnetic resonance imaging (MRI) or OCT. Elastography has been proven feasible for characterization of ocular tissues.[12–15] Acoustic radiation force optical coherence elastography (ARF-OCE) has been used in recent years for high resolution mechanical mapping.[16–21] It deploys an ultrasound transducer to perturb a tissue mechanically, while simultaneously using phase-resolved Doppler OCT to monitor the velocity of the tissue perturbation. Although mechanical quantification of the cornea has been

performed previously,[14,15] the location of the retina and its thin layers require high penetration, high resolution, and high sensitivity. These major complications have hindered previous elastography imaging techniques, and mechanical quantification of the in vivo posterior eye is presented for the first time here. A technology that enables the in vivo imaging of the posterior ocular globe is essential for gaining insight into the natural mechanical anatomy of the eye, as well as the changes that take place with ocular diseases.

In this study, ARF-OCE was used to provide phase-resolved displacement information on the central retina for a healthy and abnormal in vivo rabbit eye. Quantification of the layers uses a graph-based segmentation algorithm developed by our lab,[22] and a simple Voigt model. We demonstrated for the first time, to the best of our knowledge, an in vivo quantitative elasticity map of the retina. In addition, a general trend was observed between the healthy and the damaged rabbit retina.

Methods

Imaging System

The dual super luminescent diode (SLD) with a central wavelength of 890 nm and bandwidth of 144 nm transmits approximately 7 mW of near infrared light via an optical fiber (Fig. 1). The light first is processed through an isolator, which prohibits the back projection of light into the SLD. Then, the light is split via an optical coupler, with 80% traveling to a reference mirror, and 20% onto the sample. The power emitted onto the sample is less than 0.9 mW, which is well within the American National Standards Institute (ANSI) safety limits for ocular imaging. On the reference side, the light is collimated with a lens, attenuated via a tunable slit, and reflected from a mirror. On the sample side, the light is collimated, scanned with a galvanometer, and focused onto the sample. The scattering from both sides is transmitted back through the same fiber to the detection arm, where the interference light is collimated, the wavelength split via a diffraction grating, and the pattern focused onto the line-scan CMOS camera. The interference pattern then is processed via software and the depth information is extracted for each A-line, including the intensity and phase portions.

Rabbit Preparation

All rabbit experiments were performed with adherence to the guidelines set forth by the University of California, Irvine Institutional Animal Care and Use Committee (IACUC). To induce damage on the rabbit retina, the rabbit was treated with a high fat diet, blue light exposure, and nicotine for eight weeks total. Similar animal models using rodents and rabbits have been reported previously.[23,24] The rabbit was exposed to blue light for 2 hours a day, five times a week for eight weeks, by lining the cage with blue light light-emitting diode (LED) strips. The rabbit was imaged every 2 weeks, from weeks 0 to 9, according to the protocol, and killed. During imaging, the rabbit was first injected with 35 mg/kg ketamine and 5 mg/kg xylazine subcutaneously. For topical anesthesia, two drops of proparacaine hydrochloride was applied. Topical atropine solution also was added for dilation of the eye. Once the rabbit became unconscious, it was placed on the imaging stage and the eye was proptosed. During imaging, the heart rate and oxygen saturation levels were monitored consistently and additional anesthesia via subcutaneous injection of 17.5 mg/kg ketamine was added. After imaging, the rabbit was given buprenorphine for pain management as necessary, and was monitored closely until it became fully conscious. In the final terminal imaging, the rabbit was catheterized via the ear and injected with euthasol. OCT images from weeks 4 and 8 were compared. At the end of 8 weeks, the rabbit was imaged and euthanized. During histopathologic examination we found mononuclear round cells in a small focal accumulation in the diseased rabbit choroid. We speculated these were lymphocytes responding to the retinal injury.

Results

System Setup

A spectrometer-based OCT system with a central wavelength of 890 nm and a bandwidth of 144 nm was used for this study. A schematic diagram of the system setup is shown in Figure 1a and a close up of the imaging setup is illustrated in Figure 1b. A galvanometer scanner is used to sweep across the sample and a scan lens is used to focus the OCT light onto the retina. For the purpose of in vivo imaging, a custom phosphate-buffered saline (PBS) bath is used, where a large red ring holds a sheet of flexible latex that is filled with PBS. A small aperture is made at the bottom of the latex sheet, where it goes directly over the proptosed rabbit eye. The ultrasound transducer is used for excitation of tissue displacement, and is placed directly inside the PBS bath, which acts as a propagation medium for the ultrasound. The ring acoustic transducer is aligned to be exactly confocal with the OCT beam using a hydrophone before the experiment to ensure that data are acquired within the lateral focal region of the transducer and that maximum tissue response can be measured.

The tissue response is detected using a CMOS camera, where the interference signal is extracted through real-time processing and converted to OCT intensity images and phase-resolved displacement maps. The axial resolution of the imaging system is approximately 3 μm with a lateral resolution of 27 μm in air. The phase sensitivity of the elastography system is in the nanometer scale, which allows for high displacement contrast.

The actual setup can be visualized in the photograph shown in Figure 1c. With such an in vivo system, rapid degradation of the retina occurring in postmortem models is avoided. The rabbit is one of the few animals whose eye can be proptosed. The ring ultrasound transducer was taken out of Figure 1c so that the proptosed eye could be visible. As shown in the timing diagram in Figure 1d, the OCT detection uses C-mode to detect the mechanical response, with a line scan rate of 20 kHz, and B-frame rate of 20 frames per second. The acoustic pulse is modulated continuously during the OCT acquisition at a frequency of 833 Hz with a 50% duty cycle, which corresponds to a pulse width of 0.6 ms. The modulation pulse was chosen so that it is relatively far away from the resonance frequency of tissue, which typically is below 100 Hz, and the value corresponds to a 1.2 msec period. Other frequencies much higher than 100 Hz also would be acceptable, as long as the vibrations are slow enough to be captured by the detector. The lateral focal region was limited at approximately 400 μm to guarantee high sensitivity imaging within a uniform pressure region, while the axial focal region was extended at more than 5 mm to guarantee that the pressure distribution differs by less than 0.1 dB over the imaging depth. The acoustic intensity within the 400 μm lateral and 1 mm axial regions have been shown to be uniform, so any displacement differences in this region can be attributed to changes in mechanical properties.[18] For all experiments presented here, the central retina region 2 mm from the optical disc on the temporal side of the retina was imaged, corresponding to the area of highest visual acuity. The OCT and phase-resolved displacement information was

Investigative Ophthalmology & Visual Science

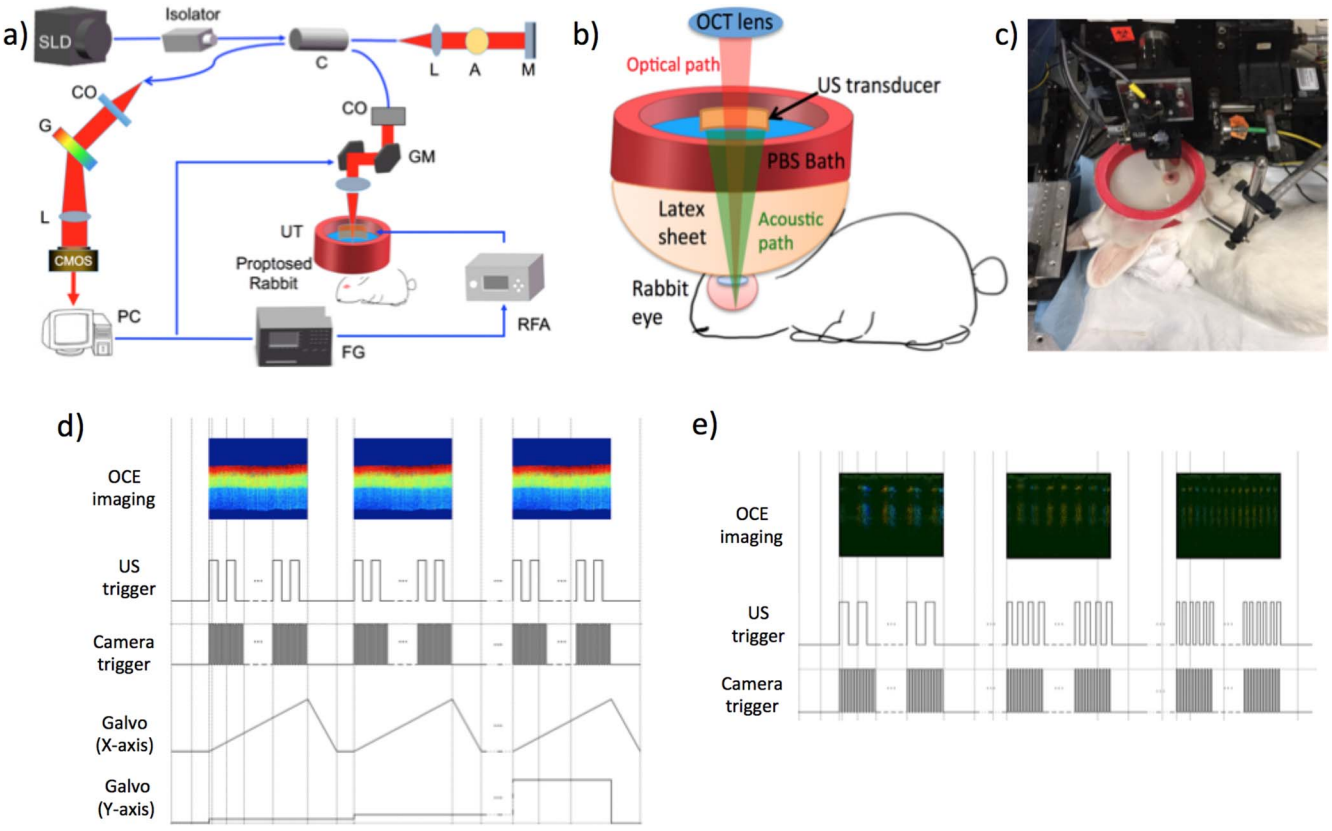

Figure 1. System setup for in vivo studies. (**a**) Schematic diagram of system. (**b**) Close up schematic of sample arm. (**c**) Photo of the setup with the rabbit eye proptosed on the stage. (**d**) Timing diagram of OCE modulation imaging. (**e**) Timing diagram of OCE frequency sweep.

obtained and recorded. The displacement information is converted to the elastic modulus with a simple Voigt model and a spring model.

The elasticity was quantitated by using the bulk frequency response of the entire depth of the posterior orbit with a simplified five-spring model to isolate individual layers, which represented the sclera, choroid, and three retinal zones as described below. Previous studies showed that the elastic modulus of the tissue is directly proportional to the square of the resonance frequency when using a Voigt body model:[17,25]

$$\mathrm{E} = \frac{\kappa L}{S} = \frac{\left(\mu^2 + \lambda^2\right) mL}{S} \qquad (1)$$

where μ is the resonance frequency, L is the thickness, m is the mass, and S is the imaging area. By sweeping the ultrasound excitation frequency, the resonance frequency μ can be found by the highest displacement and the stiffness of tissues can be calculated subsequently by Equation 1. The damping coefficient, λ, has been shown to have a trivial effect on the elasticity compared to the resonance frequency, and, therefore, can be neglected in this case.[25] The resonant frequency peak, μ, in Equation 1 is determined by doing M-mode imaging while modulating at different frequencies, and measuring the displacement level. The frequency at which the highest displacement occurs is the resonant frequency peak. In this case, a sweeping mechanism from 1 to 100 Hz has been implemented, with 0.1 Hz increments, shown in the timing diagram in Figure 1e. We used a silicone phantom with similar elasticity and thickness to the retina to calibrate the measurement of elastic modulus using Equation 1. The resonance frequency was determined to be approximately 15 Hz. The resonance frequency and the Young's modulus is related by: $\mathrm{E} = \mu^2 \times 0.03$. The bulk Young's modulus of the entire depth of the sample can be calculated to be approximately 7 kPa.

The frequency sweep method can quantify only the bulk elastic modulus of the entire imaging depth of the sample at the region of excitation. The elasticity is quantified as stress over strain, where the strain values are inversely proportional to the displacement. Because the force of the ultrasound is difficult to quantify directly, the stress on the sample cannot be quantified. The OCE images measure the displacement of the sample at each location, assuming a uniform ultrasound stress field within the transducer focal region. This means that the relative elasticity of each layer can be measured spatially according to the OCE, but the absolute Young's modulus cannot be inferred directly. It is necessary to use an additional model to calculate the individual layer elasticity.

It can be assumed that the layers of the retina, choroid, and sclera are a series of springs attached to each other with the bottommost layer fixed at a boundary. The elasticity of an individual layer can be calculated using the following spring series model,

$$\mathrm{E} = \frac{L}{\sum_{i=1}^{n} L_i / \mathrm{E}_i} \qquad (2)$$

where n is the total number of layers within the entire thickness, L, and E is the bulk elasticity of the entire region. L_i and E_i are the thickness and elastic modulus of the individual layers, respectively. In this experiment, the bulk E for the entire depth (retina, choroid, and sclera) was obtained based on the frequency sweep mechanism in Equation 1 and Figure 1e. The total thickness and thickness for individual layers were found using the segmentation algorithm on OCT B-scans. The

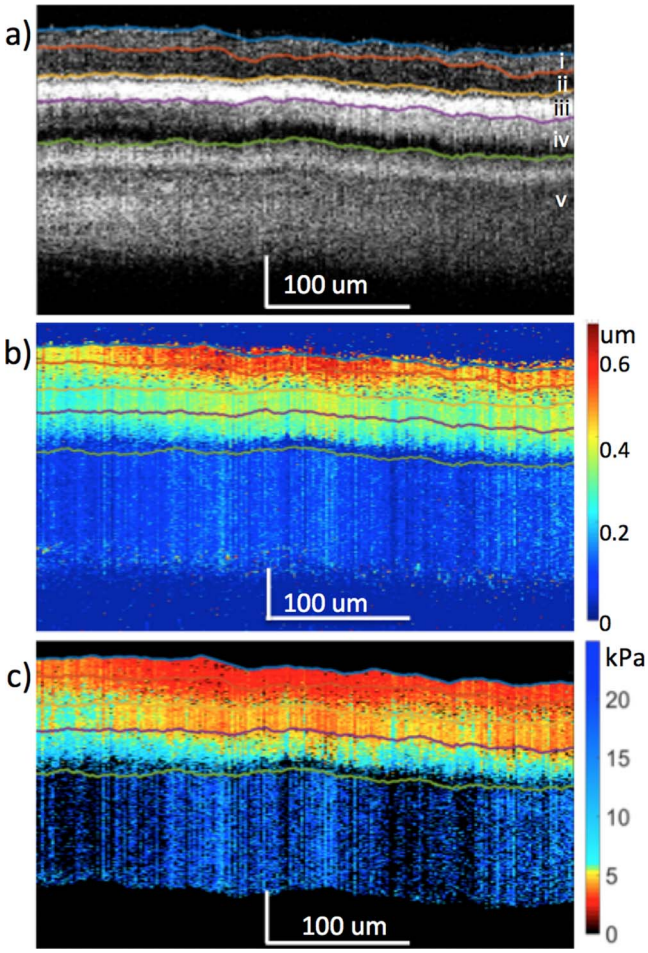

Figure 2. The in vivo rabbit posterior eye results. (**a**) OCT. (**b**) OCE displacement map. (**c**) Elastogram. *Layer i*: optic nerve fibers, ganglion cell layer, and inner plexiform layer. *Layer ii*: inner nuclear layer, outer plexiform layer, and outer nuclear layer. *Layer iii*, RPE. *Layer iv*, choroid. *Layer v*, sclera.

relative ratio of the E_i for each individual layer was determined based on the depth-dependent displacement map, as shown in Figure 1d, by using the modulated excitation approach. Finally, with the relative ratio between the layers and the quantified bulk Young's modulus, as well as the layered and bulk thicknesses, the absolute Young's modulus can be determined for each layer using Equation 2. Last, the spatial distribution of the elastic moduli can be mapped out quantitatively using the relative vibrational displacement response that is measured using ARF-OCE with the mean value based on the individual layer elasticity.

In Vivo Healthy Rabbit Study

The rabbit eye is the ideal model for this study due to the ability to proptose the eye conveniently, for bathing in ultrasonic conductive medium, such as PBS, and without inflicting damage. For translation into clinical trials, ocular gel or a waterbath with a Steri-Drape can be used to couple the ultrasonic radiation force into the retina. This is used routinely in clinical ophthalmic ultrasound, and would not be expected to be problematic for clinical translation.

The first New Zealand White rabbit, which was assumed to have a healthy ocular anatomy, was imaged. The structural resliced OCT image was obtained as shown in Figure 2a, where individual posterior layers of the eye could be isolated using the graph-based segmentation algorithm.[22] A resliced image in the y plane is used since the ultrasound excitation is synchronized in that direction, while the B-scans in the x plane displays the modulated signal. It is apparent that not all layers of the retina could be differentiated and some distortions can be seen, most likely due to the bulk motion during in vivo imaging caused by rabbit breathing or external noise as well as the limited imaging speed, which was 20 kHz. The ocular layers on the OCT were matched anatomic structures and verified by previous literature.[26] The relative OCE displacement map is shown in Figure 2b, where higher displacement was seen on the ganglion side, and decreases toward the photoreceptor side, signifying the change in relative elasticity of the different layers. The frequency response of the tissue was obtained, and the resonance frequency peak was used to calculate the bulk Young's modulus of the tissue, which was determined to be approximately 7 kPa. Using the spring model and a weighted average, the corresponding elastogram was generated in Figure 2c.

According to the OCT and elastogram results, the retinal, choroidal, and scleral layers appeared to be relatively uniform in the lateral direction, which is expected of healthy retinal tissues. Images of the OCT and OCE at different locations on the central retina within the region of ultrasound excitation are presented in Figures 3a and 3b, respectively, where similar patterns and trends can be observed across different layers. After averaging across 64 locations on the temporal retina, the mean stiffness of each layer is summarized in Figure 3c with the mean and standard deviation estimated for each layer. According to the thickness of the OCT layers and their correlation to the histologic image, the layers were matched to their respective Young's modulus. Due to the smaller thickness of the New Zealand White rabbit's posterior orbit, it was possible to obtain a signal from the choroid and sclera layers below the retina. It is important to note that tissue edema was observed in the sclera, which possibly was due to the eye proptosis as well as the constriction caused by the elastic sheet setup.

In Vivo Damaged Retinal Study

To test the feasibility of the ARF-OCE imaging system on detecting diseased states, we induced retinal damage on a second New Zealand White rabbit, primarily using blue light exposure. The rabbit was placed in a transparent chamber with 225 W of cool white LED's lining five faces of the chamber. Since cool white LED's are expected to have a high concentration of blue light in the 470's range while not causing pain to the rabbit, they are the ideal candidates.[27,28] Blue light has been shown to cause AMD in moderate amounts, and are one of the major risk factors in retinal diseases.[29,30] The 3D central retina region 2 mm away from the optic disc on the temporal side was imaged. During the first 4 weeks of treatment, no retinal damage was observed, as shown in Figures 4a and 4b. The OCT image showed a smooth transition throughout the layers, while the OCE and elastogram maps were very similar to the healthy eye from the first rabbit not damaged with light.

After 8 weeks of treatment, imaging was performed and shown in Figures 4c and 4d. The OCT image showed a dark region between the bright RPE layer and choroid, which corresponds with the detachment. There also is an irregular pocket of low scattering OCE signal in the choroid layer. In addition, it seems that the light penetration of the damaged retina is shallower than that of the relatively healthy one, as shown by the thinner section of sclera that can be observed in layer v. Histologic analysis was performed and is shown in Figures 4e and 4f. After analysis by a pathologist, it was

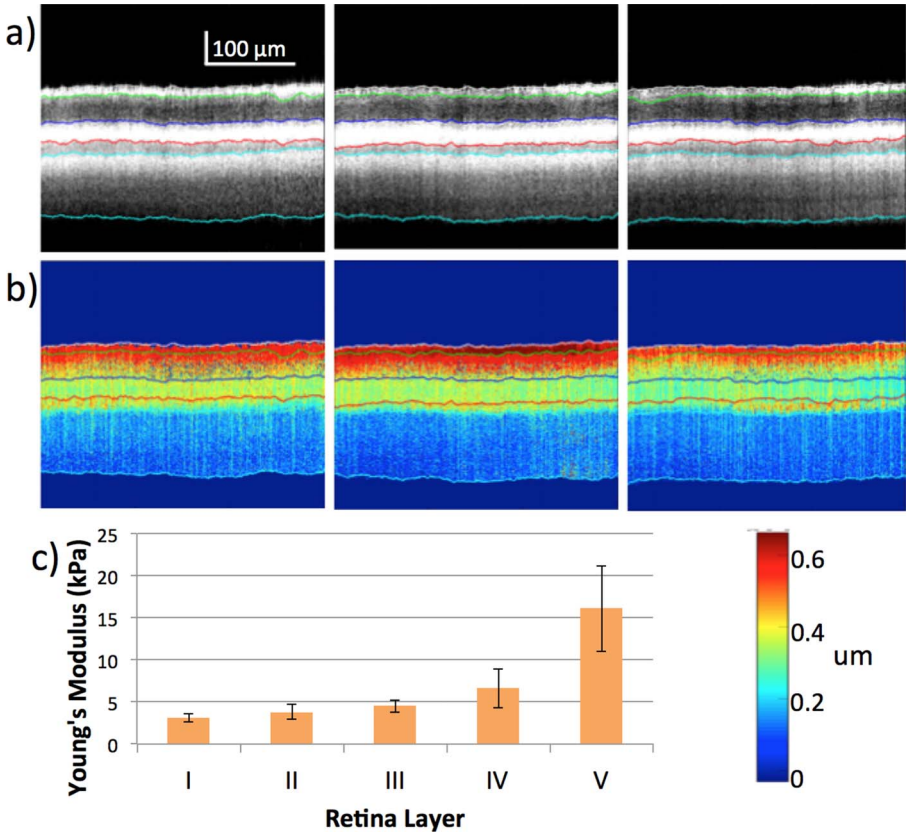

Figure 3. Posterior eye results from New Zealand White rabbit at different location in central retina. (**a**) OCT images of the central retina at increments of 75 µm within 400 µm focal region. (**b**) OCE images of corresponding region. (**c**) Summary of elasticity from layers i to v.

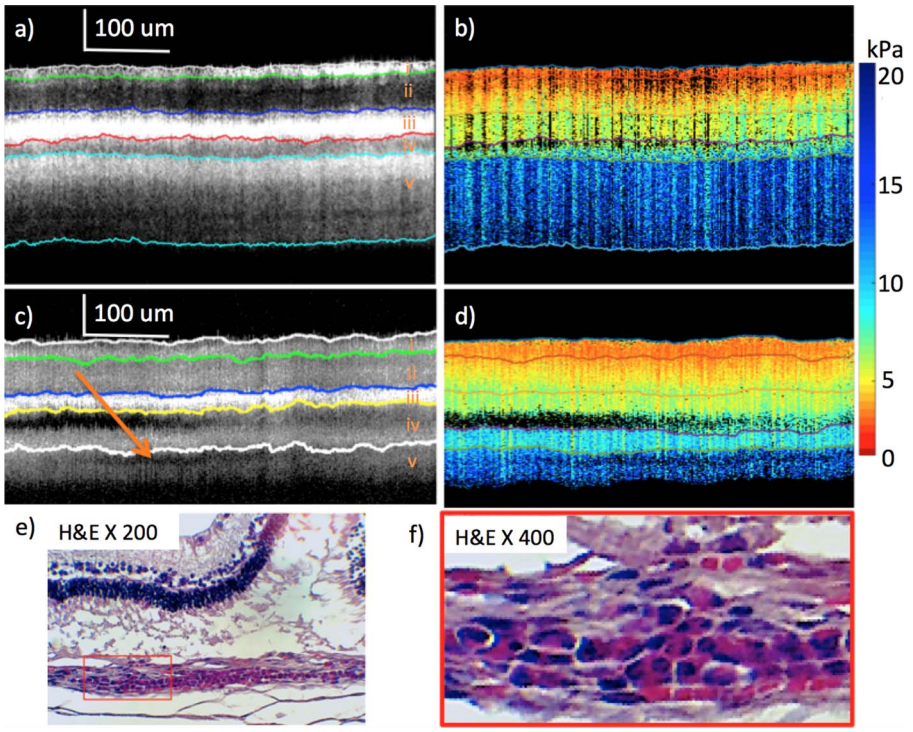

Figure 4. Healthy versus abnormal rabbit from weeks 4 and 8 imaging after light treatment. (**a**) OCT of healthy retina at week 4. (**b**) Elastogram of healthy retina at week 4. (**c**) OCT of abnormal portion of retina at week 8. (**d**) Elastogram of abnormal portion of retina at week 8. (**e**) H&E staining after euthanization at week 8. (**f**) Higher magnification, H&E histology. *Red box* includes photoreceptor/RPE debris with round cell accumulation in underlying choroid and presumed lymphocyte filtration. *Orange arrow* (**c**) points to presumed lymphocytic infiltrate in choroid, resulting in low OCT signal.

Investigative Ophthalmology & Visual Science

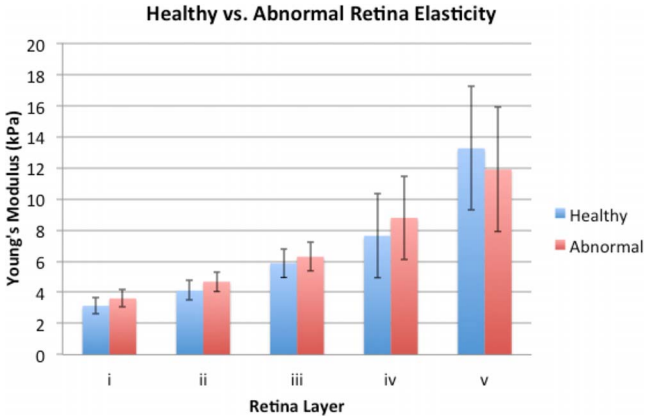

Figure 5. Histogram of relatively healthy and damaged rabbit posterior eye elasticity.

determined that inflammation was causing a presumed lymphocytic infiltrate due to the prolonged blue light exposure. From the literature, lymphocytes typically appear with a low OCT scattering signal, and inflammation can lead to reduced stiffness in the membrane.[31–33] This observation means that the low signal region on the choroid corresponds to the region of inflammation. The fold in the retina on hematoxylin and eosin staining is most likely caused by formalin fixation shrinkage artifact, as determined by the pathologist. Once again, swelling was observed in the sclera layer, which likely was caused by proptosis conditions.

Although some abnormalities were seen in the OCT, the elastogram looked very similar between the imaging performed at weeks 4 and 8. To identify differences, the Young's moduli values for each layer has been summarized in Figure 5, where the relatively healthy data at 4 weeks of treatment and the abnormal regions at week 8 are shown. An overall trend was observed where the top 4 layers generally were softer for the healthy tissue. The bottom layer was the only layer where the healthy site was stiffer than the abnormal site. According to literature, the stiffness of lymphocytes is approximately 1 kPa or even lower.[32,33] Therefore, it was likely that the lower stiffness in layer v of the abnormal rabbit was caused by infiltration of lymphocytes in the region of inflammation. One rabbit eye was analyzed using the diseased model, averaging across 500 A-lines, and while a trend was observed, the results were not statistically significant. Further in vivo studies are necessary to verify the trend across different eyes.

Discussion

Quantified elasticity maps of the in vivo posterior eye are presented for the first time to our knowledge, using a proptosed rabbit eye model. This minimally invasive technology offers high resolution and high sensitivity for penetration directly into the individual posterior eye layers. The ARF-OCE system enables in vivo imaging of the retina, which is essential for studying the retinal anatomy, as well as to detect and manage retinal diseases. The rabbit model has been used extensively in ocular studies due to its ability to be proptosed, as well as its convenience in studying small vertebrate animals. In addition to studying the pure mechanical structure of the healthy and abnormal eyes, a number of other applications can benefit from this technology. For example, in the application of the prosthetic retina using electrode stimulation, it is important to track the elasticity changes before and after stimulation, which can be done using the ARF-OCE technology.

Although we demonstrated the imaging and quantification of mechanical properties of the retina in vivo, a number of challenges must be overcome to translate the technology for clinical applications. First, the current acoustic intensity used to induce tissue motion exceeds the Food and Drug Administration (FDA) 510k guidelines for diagnostic ultrasonography of the eye. The FDA ophthalmic standard for mechanical index (MI) is 0.23 while our MI is close to 2. However, the current ARF induced displacement is hundreds of nanometers, while the phase sensitivity of our imaging system is less than 1 nm.[34] Therefore, decreasing the excitation voltage by 10-fold will be feasible, and keep the system within the safety limits. Further tests must be performed to determine the minimal excitation that is necessary to maintain adequate mechanical sensitivity. Second, the current imaging field of view is limited to below 1 mm, with the transducer excitation area as the primary limiting factor. In addition, the lateral focal region is only 400 um, it is difficult to image the entire central retina region. Adaptation of an array transducer that enables excitation at multiple locations on the retina will be necessary to image biomechanical properties of the full central retina.

In addition, during each imaging session, co-location is assured by first finding the location of the optic disk, and then moving 2 mm on the temporal side. With this method, exact alignment between each time point and correlating to histology is difficult. However, as demonstrated in Figures 3a and 3b, the retinal layer elasticity trend is quite uniform across the central retina, so the comparison between healthy and diseased models remains valid. With respect to histology, there are features that can be seen within 200 μm of the presumed region, where the histology matches with the OCT image, which is extremely helpful in co-alignment.

The condition of proptosis definitely affects the properties of the retinal layers. The scleral edema that has been observed is most likely due to scleral injection or vessel dilation resulting from proptosis. In addition, the behavior of the choroidal response pattern in proptosed versus nonproptosed eyes is drastically different.[35] Proptosis increases the IOP of the eye, which leads to choroidal edema that is likely caused by choroidal injection. Proptosis may well have an effect on layer response due to vascular congestion.[35] However, studies presented here emphasize relative changes over time or compared to normals in the proptosed state, so the results still provide valid information on relative changes. In future studies, methods for performing the procedure without proptosis are being considered, including the clinical Steri-Drape setup as well as using ultrasonic gel for index matching.

Conclusions

In this initial study, we have demonstrated the elasticity mapping of different layers in the posterior full thickness of the eye of in vivo rabbit models. The stiffness of the layers increases gradually from the ganglion side to the photoreceptor sides of the retina. In addition, we have also created a customized rabbit model primarily using blue light exposure to induce damage on the retina. Inflammation in the central retina was observed and changes in the elastic trend were speculated to be caused by the pathology. This study verified the feasibility of using ARF-OCE to provide quantified elasticity maps of the retina, and is a critical stepping stone to the clinical translation of such a technology.

Acknowledgments

The authors thank Tanya Burney for her assistance with the animal handling.

Investigative Ophthalmology & Visual Science

Supported by grants from the National Institutes of Health (Bethesda, MD, USA; R01HL-125084, R01HL-127271, R01EY-026091, R01EY021529, P41EB-015890, T32HL116270, F31EY027666), and the Air Force Office of Scientific Research (FA9550-17-1-0193).

Disclosure: **Y. Qu**, None; **Y. He**, None; **A. Saidi**, None; **Y. Xin**, None; **Y. Zhou**, None; **J. Zhu**, None; **T. Ma**, None; **R.H. Silverman**, None; **D.S. Minckler**, None; **Q. Zhou**, None; **Z. Chen**, OCT Medical Imaging, Inc. (I)

References

1. Kaiser PK, Friedman NJ, Pineda R. *The Massachusetts Eye and Ear Infirmary Illustrated Manual of Ophthalmology*. 4th ed. Philadelphia, PA: W.B. Saunders Company; 2014.
2. Jager RD, Mieler WF, Miller JW. Age-related macular degeneration. *N Engl J Med*. 2008;358:2606–2617.
3. Ayoub T, Patel N. Age-related macular degeneration. *J Roy Soc Med*. 2009;102:56–61.
4. Wong T, Chakravarthy U, Klein R, et al. The natural history and prognosis of neovascular age-related macular degeneration: a systematic review of the literature and meta-analysis. *Ophthalmology*. 2008;115:116–126.
5. Age-Related Eye Disease Study Research Group. The Age-Related Eye Disease Study system for classifying age-related macular degeneration from stereoscopic color fundus photographs: the Age-Related Eye Disease Study Report Number 6. *Am J Ophthalmol*. 2001;132:668–681.
6. Fine SL, Berger JW, Maguire MG, Ho AC. Age-related macular degeneration. *N Engl J Med*. 2000;342:483–492.
7. Spaide RF. Fundus autofluorescence and age-related macular degeneration. *Ophthalmology*. 2003;110:392–399.
8. Hee MR, Baumal CR, Puliafito CA, et al. Optical coherence tomography of age-related macular degeneration and choroidal neovascularization. *Ophthalmology*. 1996;103:1260–1270.
9. Krishnan L, Hoying JB, Nguyen H, Song H, Weiss JA. Interaction of angiogenic microvessels with the extracellular matrix. *Am J Physiol Heart Circ Physiol*. 2007;293:H3650–H3658.
10. Chen K, Rowley AP, Weiland JD. Elastic properties of porcine ocular posterior soft tissues. *J Biomed Mater Res A*. 2010;93:634–645.
11. Friberg TR, Lace JW. A comparison of the elastic properties of human choroid and sclera. *Exp Eye Res*. 1988;47:429–436.
12. Detorakis ET, Drakonaki EE, Tsilimbaris MK, Pallikaris JG, Giarmenitis S. Real-time ultrasound elastographic imaging of ocular and periocular tissues: a feasibility study. *Ophthal Surg Lasers Imag Ret*. 2010;41:135–141.
13. Litwiller DV, Lee SJ, Kolipaka A, et al. MR elastography of the ex vivo bovine globe. *J Mag Res Imag*. 2010;32:44–51.
14. Ford MR, Dupps WJ, Rollins AM, Roy AS, Hu Z. Method for optical coherence elastography of the cornea. *J Biomed Opt*. 2011;16:016005.
15. Larin KV, Sampson DD. Optical Coherence Elastography – OCT at work in tissue biomechanics. *Biomed Optics Exp*. 2017;8.2:1172–1202.
16. Qi W, Chen R, Chou L, et al. Phase-resolved acoustic radiation force optical coherence elastography. *J Biomed Opt*. 2012;17:110505.
17. Qi W, Li R, Ma T, et al. Resonant acoustic radiation force optical coherence elastography. *Appl Phys Letters*. 2013;103:103704.
18. Qu Y, Ma T, He Y, et al. Acoustic radiation force optical coherence elastography of corneal tissue. *IEEE J Select Topics Quant Electron*. 2016;22:288–294.
19. Zhu J, Qu Y, Ma T, et al. Imaging and characterizing shear wave and shear modulus under orthogonal acoustic radiation force excitation using OCT Doppler variance method. *Optics Lett*. 2015;40:2099–2102.
20. Zhu J, Qi L, Miao Y, et al. 3D mapping of elastic modulus using shear wave optical micro-elastography. *Sci Rep*. 2016;6.
21. Nguyen TM, Arnal B, Song S, Huang Z, Wang RK, O'Donnell M. Shear wave elastography using amplitude-modulated acoustic radiation force and phase-sensitive optical coherence tomography. *J Biomed Opt*. 2015;20:016001.
22. Huang S, Piao Z, Zhu J, Lu F, Chen Z. In vivo microvascular network imaging of the human retina combined with an automatic three-dimensional segmentation method. *J Biomed Opt*. 2015;20:076003.
23. Dasari B, Prasanthi JRP, Marwarha G, Singh BB, Ghribi O. Cholesterol-enriched diet causes age-related macular degeneration-like pathology in rabbit retina. *BMC Ophthalmol*. 2011;11:22.
24. Pennesi ME, Neuringer M, Courtney RJ. Animal models of age related macular degeneration. *Molec Aspects Med*. 2012;33:487–509.
25. Liang X, Oldenburg AL, Crecea V, Chaney EJ, Boppart SA. Optical micro-scale mapping of dynamic biomechanical tissue properties. *Opt Express*. 2008;16:11052–11065.
26. Cohen E, Agrawal A, Connors M, Hansen B, Charkhkar H, Pfefer J. Optical coherence tomography imaging of retinal damage in real time under a stimulus electrode. *J Neural Eng*. 2011;8:056017.
27. Kimura N, Sakuma K, Hirafune S, Asano K, Hirosaki N, Xie R. Extrahigh color rendering white light-emitting diode lamps using oxynitride and nitride phosphors excited by blue light-emitting diode. *Appl Phys Lett*. 2007;90:051109.
28. Bando K, Sakano K, Noguchi Y, Shimizu Y. Development of high-bright and pure-white LED lamps. *J Light Vis Environ*. 1998;22:2–5.
29. Taylor HR, Munoz B, West S, Bressler NM, Bressler SB, Rosenthal FS. Visible light and risk of age-related macular degeneration. *Trans Am Ophthalmol Soc*. 1990;88:163.
30. Algvere PV, Marshall J, Seregard S. Age-related maculopathy and the impact of blue light hazard. *Acta Ophthalmol Scand*. 2006;84:4–15.
31. Liu L, Gardecki JA, Nadkarni SK, et al. Imaging the subcellular structure of human coronary atherosclerosis using micro-optical coherence tomography. *Nat Med*. 2011;17:1010–1014.
32. Bufi N, Saitakis M, Dogniaux S, et al. Human primary immune cells exhibit distinct mechanical properties that are modified by inflammation. *Biophys J*. 2015;108:2181–2190.
33. Cai X, Xing X, Cai J, Chen Q, Wu S, Huang F. Connection between biomechanics and cytoskeleton structure of lymphocyte and Jurkat cells: an AFM study. *Micron*. 2010;41:257–262.
34. Zhang J, Rao B, Yu L, Chen Z. High-dynamic-range quantitative phase imaging with spectral domain phase microscopy. *Optics Lett*. 2009;34:3442–3444.
35. Silverman RH, Urs R, Lloyd HO. Effect of ultrasound radiation force on the choroid. *Invest Ophthalmol Vis Sci*. 2013;54:103–109.